Article

Ternary ACd₄P₃ (A = Na, K) Nanostructures via a Hydride Solution-Phase Route

Alan M. Medina-Gonzalez, Philip Yox, Yunhua Chen, Marquix A. S. Adamson, Maranny Svay, Emily A. Smith, Richard D. Schaller, Aaron J. Rossini, and Javier Vela*
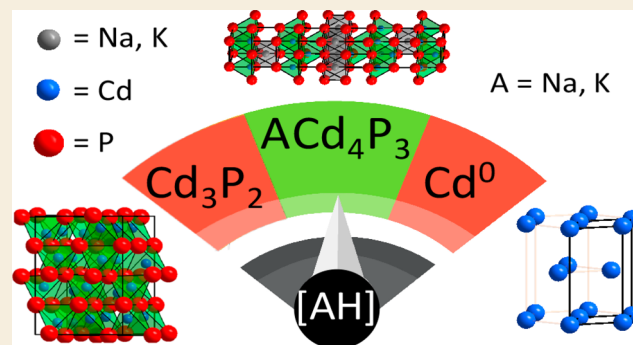
Read Online

ACCESS | Metrics & More | Article Recommendations | SI Supporting Information

ABSTRACT: Complex pnictides such as I−II₄−V₃ compounds (I = alkali metal; II = divalent transition metal; V = pnictide element) display rich structural chemistry and interesting optoelectronic properties, but can be challenging to synthesize using traditional high-temperature solid-state synthesis. Soft chemistry methods can offer control over particle size, morphology, and properties. However, the synthesis of multinary pnictides from solution remains underdeveloped. Here, we report the colloidal hot-injection synthesis of ACd₄P₃ (A = Na, K) nanostructures from their alkali metal hydrides (AH). Control studies indicate that NaCd₄P₃ forms from monometallic Cd⁰ seeds and not from binary Cd₃P₂ nanocrystals. IR and ssNMR spectroscopy reveal tri-n-octylphosphine oxide (TOPO) and related ligands are coordinated to the ternary surface. Computational studies show that competing phases with space group symmetries $R\bar{3}m$ and Cm differ by only 30 meV/formula unit, indicating that synthetic access to either of these polymorphs is possible. Our synthesis unlocks a new family of nanoscale multinary pnictide materials that could find use in optoelectronic and energy conversion devices.

KEYWORDS: I−II₄−V₃, ternary semiconductor, nanostructures, hydride, solution phase

INTRODUCTION

Pnictide compounds continue to attract significant attention because of their rich structural chemistry and because of their unique optoelectronic and catalytic properties.[1−4] Binary pnictides adopt a variety of structures with complex pnictogen motifs including tubular fragments,[5] layers,[6] clusters,[7] and cages.[8] Heavily studied ternary pnictide phases include those from the CaAl₂Si₂ and ThCr₂Si₂ type structures that exhibit potential in superconductivity,[9−11] thermoelectric,[3,4,12−14] and optical applications.[1,15] Recently reported I−II₄−V₃ compounds (I = alkali metal; II = divalent transition metal; V = pnictide) adopt a variety of related crystal structures (Figure 1), all of which share structural similarities to CaAl₂Si₂ and ThCr₂Si₂ type structures.[16−20] These Zintl phases comprise edge- and corner-sharing II−V₄ tetrahedra making up polyanionic layers. The polyanionic layers are charge-balanced by intercalated I⁺ cations (I = Na, K, Rb, or Cs). NaZn₄Sb₃ adopts a hexagonal ($P6_3/mmc$) structure and exhibits low thermal conductivity.[17] I−II₄−As₃ phases adopt orthorhombic $Pnma$ (CaFe₄As₃-type structure, e.g. KMn₄As₃), tetragonal $P4/mmm$ (KCu₄S₃-type, includes (K/Rb/Cs)Zn₄As₃, Cs(Cd/Mn)₄As₃, and RbMn₄As₃), or rhombohedral $R\bar{3}m$ (NaZn₄As₃ and (Na/K/Rb)Cd₄As₃) structures, and are studied for their magnetic and thermoelectric behavior.[16,19,20]

Interestingly, NaCd₄P₃ undergoes a phase transition from $R\bar{3}m$ to a modulated $Cm(\alpha0\gamma)s$ structure at ∼260 K.[18] With such rich structural diversity and competing binary phases, it can be challenging to synthesize these materials in a phase-pure manner.

Soft chemistry synthetic techniques can offer advantages such as the ability to prepare smaller particles with a higher surface area, as well as the ability to selectively prepare metastable or "kinetic" phases that may not be isolable through higher-temperature, solid-state reactions. In addition, the ability to control particle size and surface chemistry can play a vital role in enhancing a material's performance in solar cells, batteries, and thermoelectrics.[21−25] Examples of transition metal pnictides prepared by soft chemistry include InP and II₃−V₂ (II = Zn, Cd; V = P, As) nanocrystals, some of which are important in near-infrared (IR) imaging, detectors and lasers.[26−30] Colloidal MnPn nanocrystals (Pn = As, Sb) display ferromagnetic properties.[31,32]
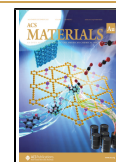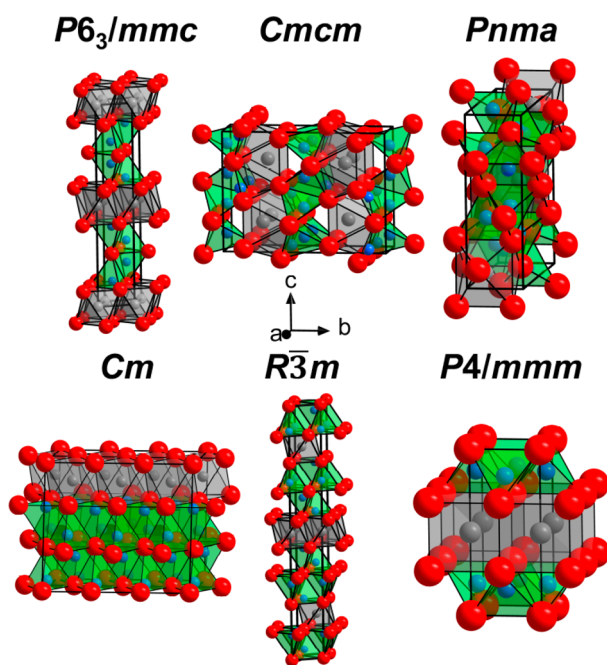
Figure 1. Unit cells of different I–II$_4$-V$_3$ phases: Hexagonal ($P6_3/mmc$), orthorhombic ($Cmcm$, $Pnma$), monoclinic (Cm), rhombohedral ($R\bar{3}m$), and tetragonal ($P4/mmm$). Colored spheres represent I (gray), II (blue), and V (red).

Developing synthetic strategies capable of producing phase-pure multinary pnictides can posit additional challenges to those observed for binary pnictides. Determining an appropriate balance between synthetic conditions and precursor reactivity is key for successful ternary formation.[33] Understanding this balance can help decode the complexity of nucleation, growth, and phase evolution of multinary nanocrystals.[34,35] Examples include I–IV–VII$_3$ (halide perovskites),[36–38] I–III–VI$_2$,[39–42] and CZTS.[43–46] Relatively few examples exist of multinary phosphides, including LiZnV (V = P, Sb) nanocrystals,[47,48] and doped Ni$_x$Co$_{2−x}$P,[49] Co$_x$Fe$_{2−x}$P,[50] and Fe$_x$Ni$_{2−x}$P[51] nanocrystals.

Herein, we report the solution-phase synthesis of ACd$_4$P$_3$ (A = Na, K) nanostructures using readily available reagents and precursors. Phase evolution and mechanistic observations pinpoint the importance of using a reducing hydride (AH) as the alkali metal precursor. Critically, we find that formation of the ternary phase proceeds from metallic (reduced) Cd seeds and not from binary Cd$_3$P$_2$ seeds. Infrared spectroscopy and solid-state NMR show that the surface of the ternary nanostructures is passivated by tri-n-octylphosphine oxide (TOPO) and related ligands. Further, we use computations to probe the energetics of polymorphism in NaCd$_4$P$_3$ and compare the results of these studies to our experimental observations.

■ RESULTS AND DISCUSSION

Hydride Synthesis

Recent reports on the colloidal synthesis of LiZnPn (Pn = P, Sb)[47,48] and NaBiE$_2$ (E = S, Se)[40,42] nanocrystals, as well as solid-state alkali zinc antimonides[17,52] rely on highly reducing conditions and reactants. Inspired by this approach, we have synthesized ACd$_4$P$_3$ (A = Na, K) nanostructures by injecting CdMe$_2$ into a hot solution of the corresponding, commercially

available alkali metal hydride (AH) in tri-n-octylphosphine (TOP) at 240 °C, followed by heating at 330 °C (Scheme 1).

Scheme 1. Solution-Phase Synthesis of I–IV$_4$–V$_3$ Nanostructures (Unbalanced)

$$AH + CdMe_2 \xrightarrow[330\ °C,\ t]{TOP} ACd_4P_3$$

$$A = Na, K$$
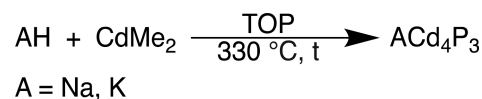
TOP was chosen as the P precursor because of its ability to act as a solvent, a surfactant, and—through thermal decomposition at this temperature—as an anionic (P$^{3−}$) precursor.[47,48,53−56]

In the case when NaH is used, powder XRD analysis of the solids isolated after 90 min of reaction (see Methods and Table 1) shows reflections that match those of bulk NaCd$_4$P$_3$ (Figure 1). The individual reflection peaks are slightly broadened, corresponding to a relatively small, single-crystalline domain (Scherrer) size of 25 ± 6 nm (Figure 2). Scanning electron microscopy (SEM) analysis shows aggregated plates and needles (Figure 3). Transmission electron microscopy (TEM) reveals that the length of the needles varies between 210−960 nm, whereas the diameter of the plates varies between 95−350 nm. The widths of both needles and plates range from 20−65 nm. Elemental analysis by energy-dispersive X-ray spectroscopy (EDS) shows the plates have a slightly lower amount of Cd—are ∼20% deficient—compared to the needles.

In the case when KH is used, powder XRD of solids isolated after 60 min reaction match the reported pattern of bulk KCd$_4$P$_3$, with a Scherrer size of 40 ± 13 nm. A small amount (∼5%) of metallic (reduced) Cd^0 and Cd$_3$P$_2$ binary is also present, the latter with a Scherrer size of 27 ± 10 nm (Table 1). In the experimental powder XRD patterns of both NaCd$_4$P$_3$ and KCd$_4$P$_3$ nanostructures, we note that the reflections at 36−37° 2θ have slightly lower intensities than expected relative to the reflections at 42−43° 2θ (Figure 1), which may be due to either preferred orientation because of their plate/needle morphology and/or sample preparation.

Solution-Phase Space

We next examined the effects of different reaction parameters on the phase evolution of ACd$_4$P$_3$ nanostructures (Figure 4). Interestingly, the exact concentration of NaH is critical to the formation of NaCd$_4$P$_3$ (see Table 1 and the Supporting Information). Using an initial cadmium concentration, [CdMe$_2$] of 0.1 mM at 330 °C, and a sodium hydride concentration, [NaH] of 0.1 mM resulted in 95% Cd$_3$P$_2$ and 5% Cd^0 after 60 min. Keeping [CdMe$_2$] and the reaction temperature both constant, we find that just tripling [NaH] to 0.3 mM results in almost phase pure, 95% NaCd$_4$P$_3$, with a small (5%) amount of Cd^0. These results strongly suggest that precise redox modulation of the reducing environment of the reaction is critical to the formation and successful isolation of ternary ACd$_4$P$_3$ nanostructures. Using a [NaH] of 0.3 mM and a [CdMe$_2$] of 0.1 mM as a set of precursor concentrations that provided the cleanest form of NaCd$_4$P$_3$—with fewer impurities—we also examined how temperature and time affect the formation of the ternary phase. Hot injection of CdMe$_2$ at 240 °C to a solution of TOP/NaH resulted in only (100%) metallic Cd^0. Increasing the temperature to 330 °C first resulted in Cd^0. However, as time progressed, NaCd$_4$P$_3$

Table 1. Solution-Phase Synthesis of NaCd$_4$P$_3$ and KCd$_4$P$_3$ Nanostructures

no.	cationic precursors (mM)	medium^a (mM)	t (min)	T (°C)	product(s) (%)
1	NaH (0.3) + CdMe$_2$ (0.1)	TOP	30	330	NaCd$_4$P$_3$ (92) + Cd (8)
2	NaH (0.3) + CdMe$_2$ (0.1)	TOP	60	330	NaCd$_4$P$_3$ (95) + Cd (5)
3	NaH (0.3) + CdMe$_2$ (0.1)	TOP	90	330	NaCd$_4$P$_3$ (97) + Cd (3)
4	NaH (0.3) + CdMe$_2$ (0.1)	TOP	1	330	Cd (100)
5	NaH (0.3) + CdMe$_2$ (0.1)	TOP	0.5	240	Cd (100)
6	NaH (0.2) + CdMe$_2$ (0.1)	TOP	60	330	Cd$_3$P$_2$ (15) + NaCd$_4$P$_3$ (81) + Cd (4)
7	NaH (0.1) + CdMe$_2$ (0.1)	TOP	60	330	Cd$_3$P$_2$ (100)
8	NaH (0.4) + CdMe$_2$ (0.1)	TOP	60	330	NaCd$_4$P$_3$ (83) + Cd (17)
9	KH (0.2) + CdMe$_2$ (0.1)	TOP	60	330	KCd$_4$P$_3$ (12) + Cd (1) + Cd$_3$P$_2$ (87)
10	KH (0.3) + CdMe$_2$ (0.1)	TOP	60	330	KCd$_4$P$_3$ (47) + Cd (10) + Cd$_3$P$_2$ (43)
11	KH (0.4) + CdMe$_2$ (0.1)	TOP	60	330	KCd$_4$P$_3$ (58) + Cd (5) + Cd$_3$P$_2$ (37)
12	KH (0.8) + CdMe$_2$ (0.1)	TOP	30	330	Cd (100)
13	KH (0.4) + CdMe$_2$ (0.1)	TOP	30	330	KCd$_4$P$_3$ (71) + Cd (19) + Cd$_3$P$_2$ (10)
14	KH (0.4) + CdMe$_2$ (0.1)	TOP	90	330	KCd$_4$P$_3$ (55) + Cd (9) + Cd$_3$P$_2$ (44)
15	K(oleate) (0.3) + CdMe$_2$ (0.1)	TOP	30	330	Cd$_3$P$_2$ (100)
16	Na(oleate) (0.3) + CdMe$_2$ (0.1)	TOP	30	330	Cd$_3$P$_2$ (100)
17	NaH (0.3) + Na(oleate) (0.02) + CdMe$_2$ (0.1)	TOP	60	330	NaCd$_4$P$_3$ (81) + Cd^0 (19)
18	NaH (0.3) + Na(oleate) (0.06) + CdMe$_2$ (0.1)	TOP	60	330	NaCd$_4$P$_3$ (70) + Cd^0 (30)
19	NaH (0.3) + CdMe$_2$ (0.1)	(TMS)$_3$P (0.8)/ODE	30	310^b	Cd^0 (97) + Cd^0 (3)
20	NaH (0.3) + CdMe$_2$ (0.1)	(PhO)$_3$P (0.8)/ODE	30	310^b	Cd$_3$P$_2$ (93) + Cd^0 (7)
21	NaBH$_4$ (0.3) + CdMe$_2$ (0.1)	TOP	90	330	Cd$_3$P$_2$ (100)
22	KBH$_4$ (0.4) + CdMe$_2$ (0.1)	TOP	60	330	Cd$_3$P$_2$ (100)
23	NaH (0.5) + CdMe$_2$ (0.1)	(TMS)$_3$P (0.1)/TOP	60	300	Cd^0 (100)
24	KH (0.4) + ZnEt$_2$ (0.1)	TOP	30	330	amorphous
25	KH (0.8) + ZnEt$_2$ (0.1)	TOP	30	330	amorphous
26	KH (0.4) + ZnEt$_2$ (0.1)	TOP	90	330	amorphous

^{a}TOP serves as anionic (P^{3-}) precursor. ^{b}Reflux of ODE occurred at this temperature.

became the main crystalline product (92% at 30 min, 97% at 90 min).

The formation and phase evolution of KCd$_4$P$_3$ nanostructures displays a similar phase space diagram relative to NaCd$_4$P$_3$ (Figure 4). While keeping the initial concentrations of [KH] at 0.2 mM and [CdMe$_2$] at 0.1 mM, and the temperature at 330 °C, we find that some (12%) KCd$_4$P$_3$ and large (87%) amounts of Cd$_3$P$_2$ are formed—along with a minimal (1%) amount of Cd^0—after 60 min of reaction (Table 1 and the Supporting Information). Under identical reaction conditions, increasing [KH] to 0.4 mM increases the amount of KCd$_4$P$_3$ to 58% and lowers the amount of Cd$_3$P$_2$ to 37% and of Cd^0 to 5%. As observed in the previous case, further increases in potassium hydride concentration, for example, to a [KH] of 0.8 mM, result in the formation of only (100%) Cd^0. This further reinforces the view that an overly reducing environment is detrimental to the stability of Cd$_3$P$_2$ or KCd$_4$P$_3$ nanomaterials. Using a [KH] of 0.4 mM and a [CdMe$_2$] of 0.1 mM at 330 °C gave the purest form of KCd$_4$P$_3$ (Figure 4, Table 1). Under these conditions, a time progression study showed that 71% KCd$_4$P$_3$, 19% Cd^0, and 10% Cd$_3$P$_2$ form after 30 min reaction, whereas 55% KCd$_4$P$_3$, 44% Cd$_3$P$_2$, and 9% Cd^0 form after 90 min.

Formation Mechanism and Ternary Phase Evolution

The different ternary, binary, and metallic phase distributions observed for similar concentrations of NaH and KH could be attributed to the relative reactivity of the two hydrides. Both KH and NaH are highly reducing, nucleophilic, and basic (pK_a ~ 35). However, according to the available standard redox potentials, KH (−2.58 V vs NHE) is slightly more reducing than NaH (−2.36 V vs NHE).[57] It is also worth noting that NaBH$_4$ and KBH$_4$ are less reactive and fail to produce ternary;

for reference, the reported standard potential of NaBH$_4$ is −1.43 V vs NHE[58,59] (Table 1; Figure 4).

To better understand the phase evolution of ACd$_4$P$_3$ nanostructures from solution, we probed the relationship between the formation of the ternary phase from the binary (Cd$_3$P$_2$) vs the metallic (Cd^0) nanophases (see Scheme 2).

Injecting CdMe$_2$ to TOP at 240 °C and raising the temperature to 330 °C for 3 min results in the formation of Cd$_3$P$_2$ binary. This allowed us to form fresh Cd$_3$P$_2$ nanocrystals in situ, without having to isolate or expose them to air/oxygen or affecting their surface ligand chemistry (TOP- vs TOPO-passivation, for example, see below). Interestingly, when in situ Cd$_3$P$_2$ is formed in this way and subjected to the aforementioned NaH/TOP conditions—[NaH] = 0.3 mM, 330 °C—the powder XRD of solids isolated from this reaction only show reflections associated with Cd^0. This strongly suggests that Cd$_3$P$_2$ nanocrystals are unstable in the presence of sufficient concentrations of NaH and are quickly reduced to metallic Cd^0. As the reaction time progresses to 60 min, NaCd$_4$P$_3$ nanostructures form and minimal Cd^0 remains. Therefore, formation of the ternary phase occurs in a stepwise manner: First, by formation of Cd^0 seeds; second, by interfacial reaction with P^{3-}—from thermal decomposition of TOP—and assembly of the resulting polyanionic [Cd$_4$P$_3$]$^-$ layers around Na$^+$ cations. This behavior is similar to that reported previously for LiZnPn (Pn = P or Sb)[47,48] or NaBiE$_2$ (E = S or Se),[42] whose phase evolution also proceeds through monometallic seeds rather than through binary phases.

Optical Spectroscopy and XPS

Extrapolating the linear region of Tauc plots[60] made from diffuse reflectance data of films of NaCd$_4$P$_3$ nanostructures yields an indirect band gap of 1.0 eV, which agree well with
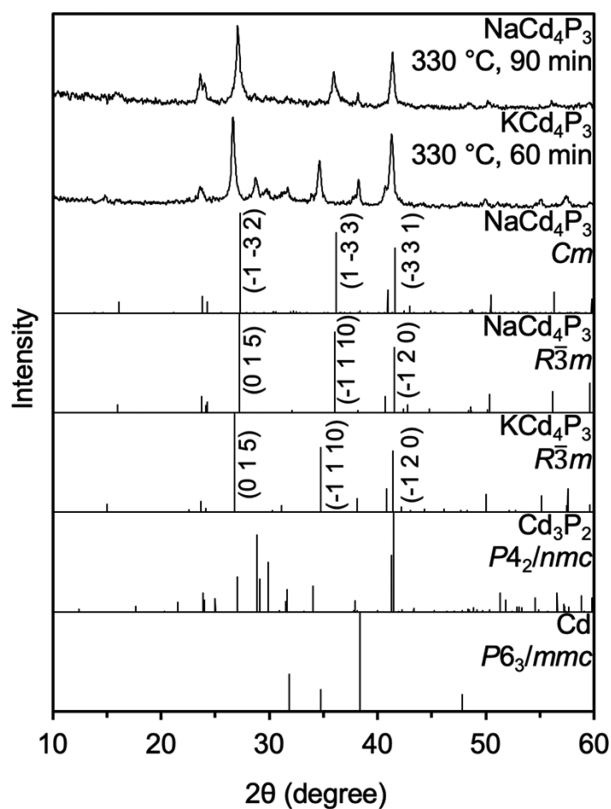
Figure 2. Powder XRD patterns of ACd_4P_3 (A = Na, K) nanostructures and relevant standards. Scherrer sizes are 25 ± 6 nm ($NaCd_4P_3$) and 40 ± 13 nm (KCd_4P_3). Miller indices for the three most intense reflections are shown. (ICSD: Cd^0 619641 ($P6_3/mmc$); Cd_3P_2 77869 ($P4_2/nmc$); $NaCd_4P_3$ ($R\bar{3}m$) 431346; $NaCd_4P_3$ (Cm) 431347; KCd_4P_3 262033 ($R\bar{3}m$)).
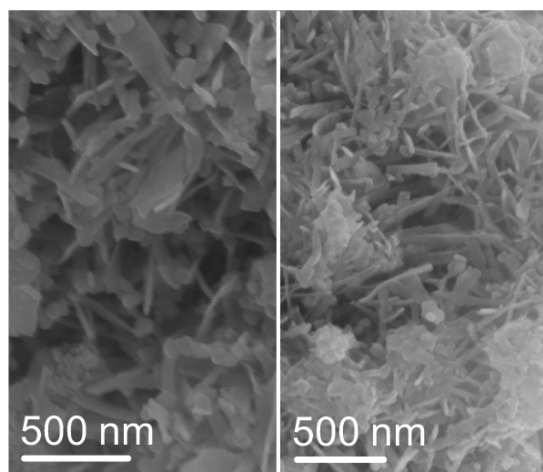

Figure 3. Representative SEM images of $NaCd_4P_3$ nanostructures showing the presence of plate and needlelike morphologies. Refer to entry 3 from Table 1. See the Supporting Information for more examples.

prior literature.[16,17] Interestingly, the photoluminescence (PL) spectra of $NaCd_4P_3$ nanostructures show peaks at 910 and 1058 nm (fwhm = 50−100 nm, QY < 0.1%). Because Cd_3P_2 has a bulk band gap of 0.55 eV (~2250 nm) but a large Bohr radius of 18 nm, it is possible that small (sub 3 nm) binary impurities may be responsible for one of the observed PL peaks.[61−66] However, we note that although the Raman
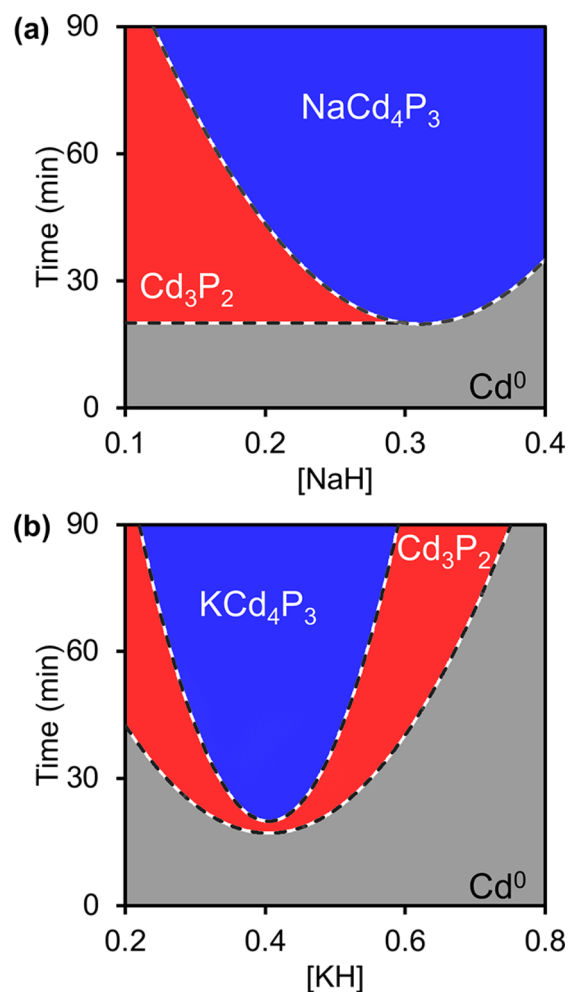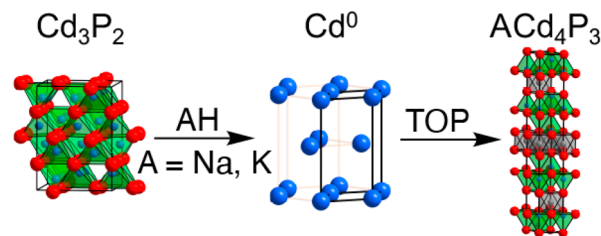

Figure 4. Solution-phase space diagram for the formation of (a) $NaCd_4P_3$, (b) KCd_4P_3, and related phases from solution. Although in some instances additional phases are present, these plots provide a general idea about the main phase produced for each set of experimental conditions.

Scheme 2. Phase Evolution of ACd_4P_3 Nanostructures (A = Na, K)[a]

[a]Color spheres are used for A (gray), Cd (blue), and P (red).

spectrum of freshly made Cd_3P_2 nanocrystals shows major bands at 347, 383, and 458 cm^{-1},[18,67] no such bands could be observed by Raman for $NaCd_4P_3$ nanostructures (see the Supporting Information).

The IR spectrum of $NaCd_4P_3$ nanostructures shows ν_{as}(C−H) and ν_s(C−H) vibrations at ~2950 cm^{-1} and δ_s(CH$_2$) at ~1450 cm^{-1}, which are typical of the alkyl chains in TOP (Supporting Information). Interestingly, we also see vibrations for ν(P=O) at 1140−1060 cm^{-1} which indicate the presence of tri-n-octylphosphine oxide.[68] The broad ν(OH) vibration at

~3300 cm^{-1} confirms exposure to moisture from air. Characteristic vibrations for $\nu(P-H)$ and $\delta(P-H)$ at ~2320 cm^{-1} and ~980 cm^{-1}, respectively, are also observed (see below). X-ray photoelectron spectroscopy (XPS) shows the presence of Na$^+$, Cd^{2+}, P^{5+}, P^{3-}, and O^{2-} surface species on NaCd$_4$P$_3$ nanostructures (see the Supporting Information). P signals at 132.5 and 129.8 eV are consistent with oxidized and reduced forms of phosphorus, and appear in a 7:3 ratio. Therefore, the isolated nanostructures are capped by TOPO and P−H containing ligands instead of TOP, likely from a combination of the mechanism of precursor decomposition and of carrying out the reaction work up in air.[69]

Solid-State NMR Spectroscopy

To further probe the identity of the surface ligands of NaCd$_4$P$_3$ nanostructures, we used ^{1}H solid-state NMR experiments (Figure 5). The main observable NMR signals cover a
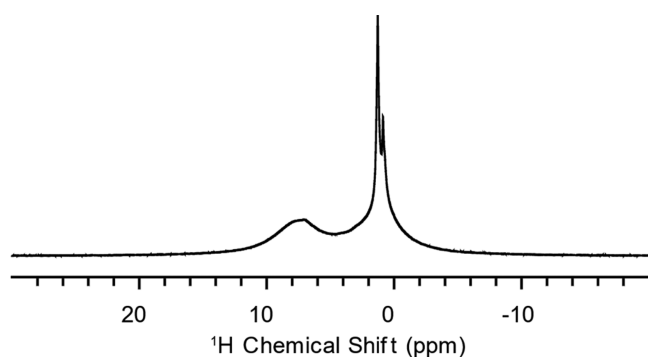

Figure 5. Magic angle spinning (MAS) ^{1}H spin echo solid-state NMR spectrum of NaCd$_4$P$_3$ nanostructures.

chemical shift range of ca. 0−4 ppm and correspond to protons from TOPO. Interestingly, another broad signal centered at ca. 7.5 ppm could indicate the presence of a phosphonate species, which may be a byproduct of the thermal decomposition of TOP during ternary synthesis.[70]

The core, surface, and subsurface ^{113}Cd and ^{31}P sites on Cd$_3$P$_2$ and Cd-InP nanocrystals were previously studied by ssNMR.[71,72] A ^{1}H → ^{31}P CP-HETCOR experiment was performed to identify surface ^{31}P sites on NaCd$_4$P$_3$ nanostructures (Figure 6). The 2D ^{1}H−^{31}P HETCOR spectrum shows an intense, relatively narrow ^{31}P NMR signal at ca. 7 ppm. There is also a broader signal that covers a chemical shift range of ca. 20−70 ppm. The peak at ca. 7 ppm is assigned to ^{31}P from phosphonate and it correlates to high-frequency ^{1}H NMR peaks at ca. 7.0 and 5.7 ppm that should correspond to O=P(H)(OH)(OR) protons from −P$\underline{H}$ and −PO$\underline{H}$, respectively. The broader ^{31}P resonance (~20−70 ppm) is assigned to ^{31}P from TOPO (O=PR$_3$) and oxidized derivatives (di-n-octylphosphinic acid and P,P′-(di-n-octyl)-pyrophosphonate); this signal correlates to ^{1}H NMR signals centered at ca. 1.5 ppm, which correspond to octyl protons.[70] Additional broadening of the signal in the region of 20−70 ppm likely arises because of bidentate and tridentate binding of oxidized TOPO derivatives.[73] These results confirm that the surface of NaCd$_4$P$_3$ nanostructures is capped by several derivatives of TOPO, as noted with other colloidal nanostructures.[70]

The ^{31}P spin echo NMR spectra show signals from all P species present in the sample, including P in the bulk of the nanostructures and surface P sites. When comparing the ^{31}P
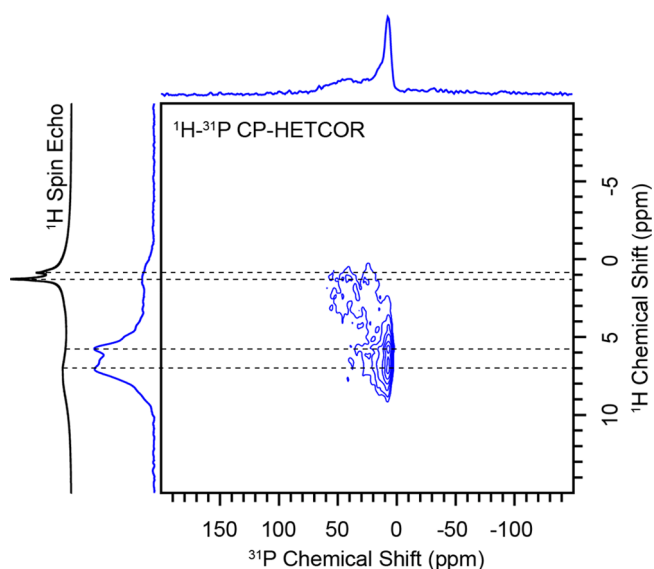

Figure 6. 2D ^{1}H → ^{31}P CP-HETCOR NMR spectrum of NaCd$_4$P$_3$ nanostructures. The CP contact time was 1 ms.

projection of the HETCOR spectrum and ^{31}P spin echo spectrum (Figure 7), the NMR signals above 0 ppm are
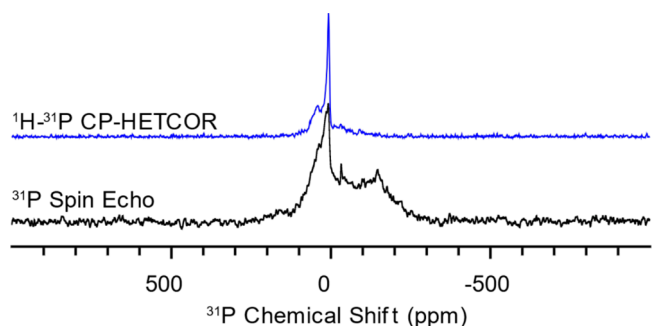

Figure 7. ^{31}P spin echo and projection of 2D ^{1}H → ^{31}P CP-HETCOR NMR spectra of NaCd$_4$P$_3$ nanostructures.

assigned to the surface P sites because these peaks are only present in the surface selective HETCOR spectrum. Other NMR signals below 0 ppm observable only in ^{31}P spin echo are assigned to the core P sites of NaCd$_4$P$_3$. We note that similarly broadened ^{31}P solid-state NMR spectra have been seen in indium phosphide, zinc phosphide and cadmium phosphide.[54,71,74,75] The broadening of ^{31}P core signals likely arises from some combination of homonuclear dipolar coupling and slight defects in bond lengths across different particle sizes and morphologies (needles and plates).

Ternary Polymorphism from Computations

As mentioned above, several polymorphs of ACd$_4$Pn$_3$ phases exist (A = Na, K, Rb) (Pn = P, As).[18] We used density functional theory (DFT) calculations to determine the thermodynamically stable phase for NaCd$_4$P$_3$. We considered four plausible structures: $P4/mmm$, $P6_3/mmc$, Cm, and $R\bar{3}m$. The $P4/mmm$ structure was determined for CsZn$_4$P$_3$ and RbZn$_4$P$_3$, whereas the $P6_3/mmc$ structure was determined for NaZn$_4$Sb$_3$.[16,18] In both cases, the structures have not been reported for NaCd$_4$P$_3$, but were considered because of their structural and compositional similarities. The $R\bar{3}m$ structure is reported as the "β phase",[18] whereas the Cm "α phase" was

reported as a modulated structure with Cd responsible for the modulation.[18] An approximation for the modulated structure was used for the computations (Figure 8 and Table 2). From
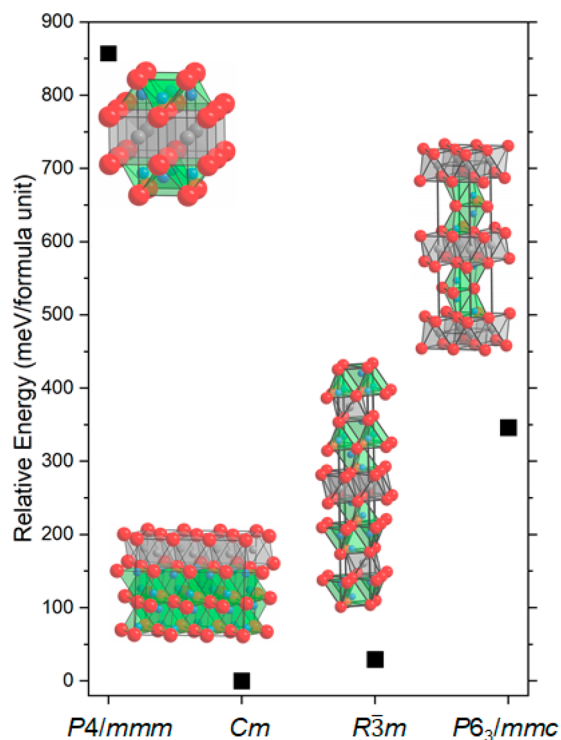

Figure 8. Calculated energies for the reported $P4/mmm$, Cm, and $R\overline{3}m$ crystal structures. The lowest energy structure is Cm, by 30 meV.

Table 2. Selected Calculations and Data for NaCd$_4$P$_3$

phase	calcd band gap (eV)	experimental band gap (eV)	energy/formula unit (meV)
$P4/mmm$	0.0		856.76
Cm	0.1		0.0
$R\overline{3}m$	0.1	1.0 (indirect)	29.33
$P6_3/mmc$	0.7		346.14

the calculated total energy of the three structures, Cm exhibits the lowest energy, with $R\overline{3}m$ being only 30 meV higher in energy. $P6_3/mmc$ and $P4/mmm$ were 350 and 850 meV higher in total energy than Cm respectively, pointing to the improbability of the structures. Using the local density approximation (LDA) tends to underestimate the unit lattice parameters and volume. Although Cm and $R\overline{3}m$ models are close in volume per formula unit (170.45 vs 170.26 Å^3), $P4/mmm$ is substantially larger (176.86 Å^3). Our results are in agreement with previous reports for this system. These show that the $R\overline{3}m$ phase converts to a modulated Cm phase reversibly at ~260 K.[18] Because the calculations are a 0 K approximation, we would expect that the Cm phase would be the lowest in energy and $R\overline{3}m$ would be close in energy. As previously reported, the density of states calculation for $R\overline{3}m$ and Cm show a small band gap (see the Supporting Information). Density of states calculations for the Cm phase show a mixing of the Cd and P in the valence band as well as the conduction band. Employing band gap calculations using LDA is known to severely underestimate band gaps.[76,77] Therefore, even though the calculated band gap for $P63/mmc$ appears closer to the experimental value, $P63/mmc$ is higher in

energy, making it an unlikely candidate for the phase observed experimentally.

CONCLUSIONS

In summary, we have explored the solution-phase synthesis, phase space diagram, and chemical spectroscopy of ACd$_4$P$_3$ nanostructures made by hot injection of dimethylcadmium to a solution of alkali metal (A = Na or K) hydride in TOP. Successful formation and isolation of ACd$_4$P$_3$ is highly dependent on the hydride concentration. We were able to identify that Cd$_3$P$_2$, a common binary impurity, is unstable in the hydride reducing environment of the reaction, quickly forming metallic cadmium. It is this metallic cadmium that serves as a seed for the formation of ternary ACd$_4$P$_3$ nanostructures. IR and 1D ^{1}H ssNMR show that TOPO and phosphonate ligands are bound to the NaCd$_4$P$_3$ surface. 2D ^{1}H → ^{31}P CP-HETCOR ssNMR shows surface signals that belong to TOPO and its derivative ligands. ^{31}P spin echo and 2D ^{1}H → ^{31}P CP-HETCOR show surface and core NaCd$_4$P$_3$ signals that are clearly different from those previously observed for Cd$_3$P$_2$. Calculations show two of four polymorphs are considered to have the lowest energies in this system, in agreement with what is observed experimentally. We believe this work represents an important leap forward into the colloidal synthesis of complex ternary nanophases, which will permit further characterization of their properties and, one day, enable their long-sought applications in fields such as thermoelectrics. We hope this work will inspire further exploration of ternary pnictide materials and other potentially useful Zintl materials.

METHODS

Materials

Sodium hydride (NaH, 99%), potassium hydride (KH, 30 wt % mineral oil), 1-octadecene (ODE, technical grade, 90%), potassium borohydride (99.9%), and dimethylcadmium (CdMe$_2$, 99%) were purchased from Sigma; tri-n-octylphosphine (TOP, 97%), sodium oleate (99%), tris(trimethylsilyl)phosphine (98%), and triphenylphosphite (97%) from Strem; potassium oleate (98%) from TCI; toluene (99.9%), hexanes (99.9%), and ethanol (99.9%) from Fisher; sodium borohydride (99.9%) from Acros. KH was washed with anhydrous hexanes three times inside a dry N$_2$-filled glovebox to remove excess mineral oil and dried under vacuum overnight. Other chemicals were used as received.

Synthesis

Synthesis of ACd$_4$P$_3$ (A = Na, K). AH (0.5−4 mmol), TOP (5 mL), and a glass coated stir bar were added to a three neck RB flask and degassed for 30 min at 120 °C. After refilling with Ar, the mixture was heated to 240 °C and CdMe$_2$ (0.5 mmol, 0.03 mL) was swiftly injected. The mixture was heated to 330 °C for the specified time.

NaCd$_4$P$_3$ Formation Mechanism. TOP (4 mL) and a glass-coated stir bar were added to a three-neck RB flask and degassed for 30 min at 120 °C. After refilling with Ar, the mixture was heated to 240 °C and CdMe$_2$ (0.5 mmol, 0.03 mL) was swiftly injected. The mixture was heated to 330 °C and a slurry of NaH (40 mg) in TOP (1 mL) was swiftly injected. Heating was continued for 60 min.

Purification. The crude solution (~1.0 mL) was diluted with toluene (~10 mL) and centrifuged at 5000 rpm for 5 min. The supernatant was discarded, and the precipitate was solubilized and diluted with toluene (~10 mL). Solids were isolated by centrifugation at 5000 rpm for 5 min. *Caution: CdMe$_2$ is highly pyrophoric and exposure to air could cause ignition.* When TOP is used as the phosphorus precursor, it is possible for PH$_3$ to form, although further investigation is needed.[53,78]

Structural and Compositional Characterization

Powder X-ray diffraction patterns were measured using Cu Kα radiation on a Rigaku Ultima IV (40 kV, 44 mA) diffractometer using a background-less quartz sample holder. Scherrer analysis and percent composition was performed with Match! (κ value of 0.9). An internal standard of silicon powder (Si^0, $a_0 = 5.43123$ Å, 640D) was used for line position and Scherrer size. Transmission electron microscopy imaging was performed on a FEI Tecnai G2-F20 scanning transmission electron microscope. Scanning electron microscopy imaging was performed using an FEI Quanta 250 field-emission SEM in the high vacuum mode. Electron-dispersive spectroscopy analysis was performed using an Oxford Aztec system. A 10 kV beam was used and both secondary and backscattered electron images were collected. A layer of 2 nm Ir was sputter-coated on the sample to avoid charging.

Spectroscopic Characterization

Diffuse-reflectance spectra were measured with an SL1 tungsten halogen lamp (vis-IR), an SL3 deuterium lamp (UV), and a BLACK-Comet C-SR-100 spectrometer. Samples were prepared by drop-casting hexane solutions onto glass slides. Band gap values were estimated by extrapolating the linear slope of Tauc plots by plotting $(Ah\nu)^{1/r}$ vs $h\nu$ where A = absorbance, $h\nu$ = incident photon energy in eV, $r = 1/2$ for direct and $r = 2$ for indirect semiconductors. Infrared (IR) spectroscopy measurements were performed on a Bruker Tensor 37 Fourier transform IR spectrophotometer (64 scans, transmittance mode, 4 cm^{-1} resolution). Photoluminescence measurements were performed using a 10 mW, 450 nm laser. Light, collected from the sample using an off-axis parabolic mirror, was directed to a 0.3m spectrograph and detected on a liquid-nitrogen-cooled InGaAs array (Princeton Instruments). Raman spectroscopy measurements were collected using an XploRA Plus confocal Raman microscope (HORIBA Scientific, Edison, NJ) equipped with a 20× (0.40 NA) long working distance objective in the spectral range of 50−750 cm^{-1}. An excitation laser of 532 nm operating at 4 mW with an acquisition time of 200 s was used to analyze an average of seven areas throughout the sample with three accumulations averaged per spectrum. The acquired data were plotted with IGOR (WaveMetrics, Portland, OR).

NMR Spectroscopy. All moderate field [$B_0 = 9.4$ T, $\nu_0(^1H) = 400$ MHz and $\nu_0(^{31}P) = 161.9$ MHz] solid-state NMR (SSNMR) experiments were performed on a Bruker Avance III HD spectrometer with a wide-bore magnet. A Bruker 2.5 mm $^1H-^{31}P-^{13}C$ triple-resonance MAS probe was used to perform all MAS experiments at a spinning rate (ν_{rot}) of 25 kHz. ^1H NMR shifts were referenced to neat tetramethylsilane using adamantane [$\delta_{iso}(^1H) = 1.82$ ppm] as a secondary standard. Previously published relative NMR frequencies were used to indirectly reference ^{31}P chemical shifts.[79] All experiments were performed using optimum recycle delays of $1.3 \times T_1$. All the NMR spectra were processed in Topspin 3.6. ^1H SSNMR. ^1H MAS NMR spectra were acquired using a spin echo sequence with $\pi/2$ and π pulses of 2.5 and 5 μs, respectively. ^1H radiofrequency (RF) fields were calibrated directly on each sample. ^{31}P SSNMR. ^{31}P MAS NMR spectra were acquired using a spin echo sequence with $\pi/2$ and π pulse lengths of 2.5 and 5.0 μs, respectively. The recycle delay is 10 s. $^1H \rightarrow {}^{31}P$ CP-HETCOR experiments used spin lock pulses with RF fields at 86 kHz RF and 134 kHz RF for ^1H and ^{31}P, respectively, and contact time was 1 ms. SPINAL-64 heteronuclear decoupling[80] was applied with an ^1H RF field of ca. 100 kHz. eDUMBO$_{1-22}$ homonuclear dipolar decoupling[81] was applied during the indirect ^1H dimension evolution to improve ^1H resolution in the $^1H \rightarrow {}^{31}P$ CP-HETCOR experiments. The initial phase and offset of eDUMBO$_{1-22}$ was optimized directly on each sample and used 32 μs pulse durations and 100 kHz RF fields.

Calculations

Total energy calculations were performed using the *Vienna Ab-initio Simulation Package* (*VASP*). The projected augmented-wave (PAW) pseudopotentials with the local density approximation (LDA) were used with a cutoff energy of 500 eV and a convergence energy of 1×10^{-4} eV. The tetrahedron method with Blöchl corrections were used with a dense k-point mesh when calculating total energy. Even though this level of theory often severely underestimates band gaps and can underestimate lattice parameters, the relative energies are robust when compared with other methods.[82] NaCd$_4$P$_3$ in $P4/mmm$ symmetry used a $16 \times 16 \times 12$ k-point mesh. NaCd$_4$P$_3$ in Cm symmetry used a k-point mesh of $14 \times 10 \times 10$. NaCd$_4$P$_3$ in $R\bar{3}m$ symmetry used a k-point mesh of $26 \times 26 \times 7$. NaCd$_4$P$_3$ in $P6_3/mmc$ symmetry used a k-point mesh of $26 \times 26 \times 6$. Unit cell volume, cell shape, and atomic positions were relaxed sequentially, then simultaneously. DOS calculations were then performed after convergence of the relaxations.

■ ASSOCIATED CONTENT

ⓈⒾ Supporting Information

The Supporting Information is available free of charge at https://pubs.acs.org/doi/10.1021/acsmaterialsau.1c00018.

Crystal structures, XRD, IR, EDS, TEM, SEM, FFT, diffuse reflectance, Tauc plot, density of states, Raman scattering, XPS, and photoluminescence (PDF)

■ AUTHOR INFORMATION

Corresponding Author

Javier Vela − *Department of Chemistry and Ames Laboratory, Iowa State University, Ames, Iowa 50011, United States;* ⓞ orcid.org/0000-0001-5124-6893; Email: vela@iastate.edu

Authors

Alan M. Medina-Gonzalez − *Department of Chemistry, Iowa State University, Ames, Iowa 50011, United States*

Philip Yox − *Department of Chemistry, Iowa State University, Ames, Iowa 50011, United States;* ⓞ orcid.org/0000-0002-8524-8202

Yunhua Chen − *Department of Chemistry and Ames Laboratory, Iowa State University, Ames, Iowa 50011, United States*

Marquix A. S. Adamson − *Department of Chemistry, Iowa State University, Ames, Iowa 50011, United States*

Maranny Svay − *Department of Chemistry, Iowa State University, Ames, Iowa 50011, United States*

Emily A. Smith − *Department of Chemistry and Ames Laboratory, Iowa State University, Ames, Iowa 50011, United States;* ⓞ orcid.org/0000-0001-7438-7808

Richard D. Schaller − *Department of Chemistry, Northwestern University, Evanston, Illinois 60208, United States; Center for Nanoscale Materials, Argonne National Laboratory, Lemont, Illinois 60439, United States;* ⓞ orcid.org/0000-0001-9696-8830

Aaron J. Rossini − *Department of Chemistry and Ames Laboratory, Iowa State University, Ames, Iowa 50011, United States;* ⓞ orcid.org/0000-0002-1679-9203

Complete contact information is available at:
https://pubs.acs.org/10.1021/acsmaterialsau.1c00018

Notes

The authors declare no competing financial interest.

■ ACKNOWLEDGMENTS

■ REFERENCES

(1) Cameron, J. M.; Hughes, R. W.; Zhao, Y.; Gregory, D. H. Ternary and Higher Pnictides; Prospects for New materials and Applications. *Chem. Soc. Rev.* **2011**, *40*, 4099−4118.

(2) Ovchinnikov, A.; Bobev, S. Zintl Phases with Group 15 Elements and the Transition Metals: A Brief Overview of Pnictides with Diverse and Complex Structures. *J. Solid State Chem.* **2019**, *270*, 346−359.

(3) Zeier, W. G.; Zevalkink, A.; Gibbs, Z. M.; Hautier, G.; Kanatzidis, M. G.; Snyder, J. G. Thinking Like a Chemist: Intuition in Thermoelectric Materials. *Angew. Chem., Int. Ed.* **2016**, *55*, 6826−6841.

(4) Kauzlarich, S. M.; Zevalkink, A.; Toberer, E.; Snyder, G. J.; Zintl Phases: Recent Developments in Thermoelectric and Future Outlook. In *Thermoelectric Materials and Devices*; Elsevier, 2016; Chapter 1, p 1.

(5) Lange, S.; Bawohl, M.; Weihrich, R.; Nilges, T. Mineralization Routes to Polyphosphides: Cu_2P_{20} and Cu_5InP_{16}. *Angew. Chem., Int. Ed.* **2008**, *47*, 5654−5657.

(6) Yang, Y.; Tian, N.; Zhang, Y.; Liu, D.; Zhang, D.; Chang, K.; Yan, H. Rediscovering the MP_{15} Family (M = Li, Na, and K) as an Anisotropic Layered Semiconducting Material. *J. Phys. Chem. Lett.* **2018**, *9*, 732−738.

(7) Scharfe, S.; Kraus, F.; Stegmaier, S.; Schier, A.; Fässler, T. F. Zintl Ions, Cage Compounds, and Intermetalloid Clusters of Group 14 and Group 15 Elements. *Angew. Chem., Int. Ed.* **2011**, *50*, 3630−3670.

(8) Turbervill, R. S. P.; Goicoechea, J. M. From Clusters to Unorthodox Pnictogen Sources: Solution Phase Reactivity of $[E_7]^{3-}$ (E = P−Sb) Anions. *Chem. Rev.* **2014**, *114*, 10807−10828.

(9) Kamihara, Y.; Watanabe, T.; Hirano, M.; Hosono, H. Iron-Based Layered Superconductor $La[O_{1-x}F_x]FeAs$ (x = 0.05−0.12) with T_c = 26 K. *J. Am. Chem. Soc.* **2008**, *130* (11), 3296−3297.

(10) Rotter, M.; Tegel, M.; Johrendt, D. Superconductivity at 38 K in the Iron Arsenide $(Ba_{1-x}K_x)Fe_2As_2$. *Phys. Rev. Lett.* **2008**, *101*, 107006.

(11) Wen, H.-H.; Li, S. Materials and Novel Superconductivity in Iron Pnictide Superconductors. *Annu. Rev. Condens. Matter Phys.* **2011**, *2*, 121−140.

(12) Gascoin, F.; Ottensmann, S.; Stark, D.; Haïle, S. M.; Snyder, G. J. Zintl Phases as Thermoelectric Materials: Tuned Transport Properties of the Compounds $Ca_xYb_{1-x}Zn_2Sb_2$. *Adv. Funct. Mater.* **2005**, *15*, 1860−1864.

(13) Kauzlarich, S. M.; Brown, S. R.; Snyder, J. G. Zintl Phases for Thermoelectric Devices. *Dalton Trans.* **2007**, 2099−2107.

(14) Kunioka, H.; Kihou, K.; Kato, D.; Usui, H.; Iida, Y.; Nishiate, H.; Kuroki, K.; Yamamoto, A.; Lee, C.-H. Thermoelectric Properties of $(Ba,K)Zn_2As_2$ Crystallized in the $ThCr_2Si_2$-type Structure. *Inorg. Chem.* **2020**, *59*, 5828−5834.

(15) Zhang, S.; Yan, Z.; Li, Y.; Chen, Z.; Zeng, H. Atomically Thin Arsenene and Antimonene: Semimetal-Semiconductor and Indirect-Direct Band-Gap Transitions. *Angew. Chem., Int. Ed.* **2015**, *54*, 3112−3115.

(16) He, H.; Tyson, C.; Bobev, S. Eight-Coordinated Arsenic in the Zintl Phases $RbCd_4As_3$ and $RbZn_4As_3$: Synthesis and Structural Characterization. *Inorg. Chem.* **2011**, *50*, 8375−8383.

(17) Gvozdetskyi, V.; Owens-Baird, B.; Hong, S.; Cox, T.; Bhaskar, G.; Harmer, C.; Sun, Y.; Zhang, F.; Wang, C.-Z.; Ho, K.-M.; Zaikina, J. V. From $NaZn_4Sb_3$ to HT-$Na_{1-x}Zn_4$-ySb_3: Panoramic Hydride Synthesis, Structural Diversity, and Thermoelectric Properties. *Chem. Mater.* **2019**, *31*, 8695−8707.

(18) Grotz, C.; Baumgartner, M.; Freitag, K. M.; Baumer, F.; Nilges, T. Polymorphism in Zintl Phases ACd_4Pn_3: Modulated Structures of $NaCd_4Pn_3$ with Pn = P, As. *Inorg. Chem.* **2016**, *55*, 7764−7776.

(19) Ishida, J.; Iimura, S.; Hosono, H. Structural Series in Ternary A-Mn-As Systems (A = Alkali Metal): Double-Layer-Type $CdMn4As3$ and $RbMn_4As_3$ and Tunnel-Type KMn_4As_3. *Inorg. Chem.* **2018**, *57*, 4997−5003.

(20) Pandey, A.; Samal, S. L.; Johnston, D. C. $CsMn_4As_3$: A Layered Tetragonal Transition-Metal Pnictide Compound with an Antiferromagnetic Ground State. *Inorg. Chem.* **2018**, *57*, 3206−3214.

(21) Sargent, E. H. Colloidal Quantum Dot Solar Cells. *Nat. Photonics* **2012**, *6*, 133−135.

(22) Nugraha, M. I.; Kim, H.; Sun, B.; Haque, M. A.; Arquer, F. P. G.; Villalva, D. R.; El-Labban, A.; Sargent, E. H.; Alshareef, H. N.; Baran, D. Low-Temperature-Processed Colloidal Quantum Dots as Building Blocks for Thermoelectrics. *Adv. Energy Mater.* **2019**, *9*, 1803049.

(23) Li, H.; Li, Q.; Wen, P.; Williams, T. B.; Adhikari, S.; Dun, C.; Lu, C.; Itanze, D.; Jiang, L.; Carroll, D. L.; Donati, G. L.; Lundin, P. M.; Qiu, Y.; Geyer, S. M. Colloidal Cobalt Phosphide Nanocrystals as Trifunctional Electrocatalyst for Overall Water Splitting Powered by a Zinc-Air Battery. *Adv. Mater.* **2018**, *30*, 1705796.

(24) Carey, G. H.; Abdelhady, A. L.; Ning, Z.; Thon, S. M.; Bakr, O. M.; Sargent, E. H. Colloidal Quantum Dot Solar Cells. *Chem. Rev.* **2015**, *115*, 12732−12763.

(25) Nag, A.; Kovalenko, M. V.; Lee, J.-S.; Liu, W.; Spokoyny, B.; Talapin, D. V. Metal-Free Inorganic Ligands for Colloidal Nanocrystals: S^{2-}, HS^-, Se^{2-}, HSe^-, Te^{2-}, HTe^-, TeS_3^-, OH^-, and NH_2^-, as Surface Ligands. *J. Am. Chem. Soc.* **2011**, *133*, 10612−10620.

(26) Gaponik, N.; Hickey, S. G.; Dorfs, D.; Rogach, A. L.; Eychmüller, A. Progress in the Light Emission of Colloidal Semiconductor Nanocrystals. *Small* **2010**, *6*, 1364−1378.

(27) Li, H.; Jia, C.; Meng, X.; Li, H. Chemical Synthesis and Applications of Colloidal Metal Phosphide Nanocrystals. *Front. Chem.* **2019**, *6*, 652.

(28) Shi, Y.; Zhang, B. Recent Advances in Transition Metal Phosphides Nanomaterials: Synthesis and Application in Hydrogen Evolution Reaction. *Chem. Soc. Rev.* **2016**, *45*, 1529−1541.

(29) Liu, Z.; Kumbhar, A.; Xu, D.; Zhang, J.; Sun, Z.; Fang, J. Coreduction Colloidal Synthesis of III-V Nanocrystals: The Case of InP. *Angew. Chem., Int. Ed.* **2008**, *47*, 3540−3542.

(30) Xie, R.; Battaglia, D.; Peng, X. Colloidal InP Nanocrystals as Efficient Emitters Covering Blue to Near-Infrared. *J. Am. Chem. Soc.* **2007**, *129*, 15432−15433.

(31) Senevirathne, K.; Tackett, R.; Kharel, P. R.; Lawes, G.; Somaskandan, K.; Brock, S. L. Discrete, Dispersible MnAs Nanocrystals from Solution Methods: Phase Control on the Nanoscale and Magnetic Consequences. *ACS Nano* **2009**, *3*, 1129−1138.

(32) Hettiarachchi, M. A.; Abdelhamid, E.; Nadgorny, B.; Brock, S. L. Synthesis of Colloidal MnSb Nanoparticles: Consequences of Size and Surface Characteristics on Magnetic Properties. *J. Mater. Chem. C* **2016**, *4*, 6790.

(33) Martinolich, A. J.; Neilson, J. R. Toward Reaction-by-Design: Achieving Kinetic Control of Solid-State Chemistry with Metathesis. *Chem. Mater.* **2017**, *29*, 479−489.

(34) Miller, R. C.; Neilson, J. R.; Prieto, A. L. Amide-Assisted Synthesis of Iron Germanium Sulfide (Fe_2GeS_4) Nanostars: The Effect of $LiN(SiMe_3)_2$ on Precursor Reactivity for Favoring Nanoparticle Nucleation or Growth. *J. Am. Chem. Soc.* **2020**, *142*, 7023−7035.

(35) Lee, J. M.; Miller, R. C.; Moloney, L. J.; Prieto, A. L. The Development of Strategies for Nanoparticle Synthesis: Considerations for Deepening Understanding of Inherently Complex Systems. *J. Solid State Chem.* **2019**, *273*, 243−286.

(36) Xiang, W.; Tress, W. Review on Recent Progress of All-Inorganic Metal Halide Perovskites and Solar Cells. *Adv. Mater.* **2019**, *31*, 1902851.

(37) Hong, K.; Le, Q. V.; Kim, S. Y.; Jang, H. W. Low-Dimensional Halide Perovskites: Review and Issues. *J. Mater. Chem. C* **2018**, *6*, 2189−2209.

(38) Zhou, Y.; Zhao, Y. Chemical Stability and Instability of Inorganic Halide Perovskites. *Energy Environ. Sci.* **2019**, *12*, 1495−1511.

(39) Morelli, D. T.; Jovovic, V.; Heremans, J. P. Intrinsically Minimal Thermal Conductivity in Cubic I-V-VI$_2$ Semiconductors. *Phys. Rev. Lett.* **2008**, *101*, 035901.

(40) Medina-Gonzalez, A. M.; Rosales, B. A.; Hamdeh, U.; Panthani, M. G.; Vela, J. Surface Chemistry of Ternary Nanocrystals: Engineering the Deposition of Conductive NaBiS$_2$ Films. *Chem. Mater.* **2020**, *32*, 6085−6096.

(41) Zhou, B.; Li, M.; Wu, Y.; Yang, C.; Zhang, W.-H.; Li, C. Monodisperse AgSbS$_2$ Nanocrystals: Size-Control Strategy, Large-Scale Synthesis, and Photoelectrochemistry. *Chem. - Eur. J.* **2015**, *21*, 11143−11151.

(42) Rosales, B. A.; White, M. A.; Vela, J. Solution-Grown Sodium Bismuth Dichalcogenides: Toward Earth-Abundant, Biocompatible Semiconductors. *J. Am. Chem. Soc.* **2018**, *140*, 3736−3742.

(43) Akhavan, V. A.; Goodfellow, B. W.; Panthani, M. G.; Steinhagen, C.; Harvey, T. B.; Stolle, C. J.; Korgel, B. A. Colloidal CIGS and CZTS Nanocrystals: A Precursor Route to Printed Photovoltaics. *J. Solid State Chem.* **2012**, *189*, 2−12.

(44) Pal, K.; Singh, P.; Bhaduri, A.; Thapa, K. B. Current Challenges and Future Prospects for a Highly Efficient (>20%) Kesterite CZTS Solar Cell: A Review. *Sol. Energy Mater. Sol. Cells* **2019**, *196*, 138−156.

(45) Regulacio, M. D.; Ye, C.; Lim, S. H.; Bosman, M.; Ye, E.; Chen, S.; Xu, Q.-H.; Han, M.-Y. Colloidal Nanocrystals of Wurtzite-Type Cu$_2$ZnSnS$_4$: Facile Noninjecting Synthesis and Formation Mechanism. *Chem. - Eur. J.* **2012**, *18*, 3127−3131.

(46) Thompson, M. J.; Ruberu, T. P. A.; Blakeney, K. J.; Torres, K. V.; Dilsaver, P. S.; Vela, J. Axial Composition Gradients and Phase Segregation Regulate the Aspect Ratio of Cu$_2$ZnSnS$_4$ Nanorods. *J. Phys. Chem. Lett.* **2013**, *4*, 3918−3923.

(47) White, M. A.; Baumler, K. J.; Chen, Y.; Venkatesh, A.; Medina-Gonzalez, A. M.; Rossini, A. J.; Zaikina, J. V.; Chan, E. M.; Vela, J. Expanding the I-II-V Phase Space: Soft Synthesis of Polytypic Ternary and Binary Zinc Antimonides. *Chem. Mater.* **2018**, *30*, 6173−6182.

(48) White, M. A.; Thompson, M. J.; Miller, G. J.; Vela, J. Got LiZnP? Solution Phase Synthesis of Filled Tetrahedral Semiconductors in the Nanoregime. *Chem. Commun.* **2016**, *52*, 3497−3499.

(49) Liu, J.; Wang, Z.; David, J.; Llorca, J.; Li, J.; Yu, X.; Shavel, A.; Arbiol, J.; Meyns, M.; Cabot, A. Colloidal Ni$_{2−x}$Co$_x$P nanocrystals for the hydrogen evolution reaction. *J. Mater. Chem. A* **2018**, *6*, 11453−11462.

(50) Li, D.; Arachchige, M. P.; Kulikowski, B.; Lawes, G.; Seda, T.; Brock, S. L. Control of Composition and Size in Discrete Co$_x$Fe$_{2−x}$P Nanocrystals: Consequences for Magnetic Properties. *Chem. Mater.* **2016**, *28*, 3920−3927.

(51) Shin, D.; Kim, H. J.; Kim, M.; Shin, D.; Kim, H.; Song, H.; Choi, S.-I. Fe$_x$Ni$_{2-x}$P Alloy Nanocatalyst with Electron-Deficient Phosphorus Enhancing the Hydrogen Evolution Reaction in Acidic Media. *ACS Catal.* **2020**, *10*, 11665−11673.

(52) Cox, T.; Gvozdetskyi, V.; Owens-Baird, B.; Zaikina, J. V. Rapid Phase Screening via Hydride Route: A Discovery of K$_{8−x}$Zn$_{18+3x}$Sb$_{16}$. *Chem. Mater.* **2018**, *30*, 8707−8715.

(53) Henkes, A. E.; Schaak, R. E. Trioctylphosphine: A General Phosphorus Source for the Low-Temperature Conversion of Metals into Metal Phosphides. *Chem. Mater.* **2007**, *19*, 4234−4242.

(54) Mobarok, M. H.; Luber, E. J.; Bernard, G. M.; Peng, L.; Wasylishen, R. E.; Buriak, J. M. Phase-Pure Crystalline Zinc Phosphide nanoparticles: Synthetic Approaches and Characterization. *Chem. Mater.* **2014**, *26*, 1925−1935.

(55) Senevirathne, K.; Burns, A. W.; Bussell, M. E.; Brock, S. L. Synthesis and Characterization of Discrete Nickel Phosphide Nanoparticles: Effect of Surface Ligation Chemistry on Catalytic

Hydrodesulfurization of Thiophene. *Adv. Funct. Mater.* **2007**, *17*, 3933−3939.

(56) Muthuswamy, E.; Kharel, P. R.; Lawes, G.; Brock, S. L. Control of Phase in Phosphide Nanoparticles Produced by Metal Nanoparticle Transformation: Fe$_2$P and FeP. *ACS Nano* **2009**, *3*, 2383−2393.

(57) Bratsch, S. G. Standard Electrode Potentials and Temperature Coefficients in Water at 298.15K. *J. Phys. Chem. Ref. Data* **1989**, *18*, 1−21.

(58) Šljukić, B.; Santos, D. M. F.; Sequira, C. A. C.; Banks, C. E. Analytical Monitoring of Sodium Borohydride. *Anal. Methods* **2013**, *5*, 829−839.

(59) Shen, J.; Li, Z.; Wang, Q.; Chen, Y. Chemically Prepared Fe−B Ultrafine Amorphous Alloy Particles of the way of Mixing Reactants. *J. Mater. Sci.* **1997**, *32*, 749−753.

(60) Viezbicke, B. D.; Patel, S.; Davis, B. E.; Birnie, D. P III Evaluation of the Tauc Method for Optical Absorption Edge Determination: ZnO Thin Films as a Model System. *Phys. Status Solidi B* **2015**, *252*, 1700−1710.

(61) Lin-Chung, P. J. Energy Band Structures of Cd$_3$P$_2$ and Zn$_3$P$_2$. *Phys. Status Solidi B* **1971**, *47*, 33.

(62) Sierański, K.; Szatkowski, J.; Misiewicz, J. Semiempirical Tight-Binding Band Structure of II$_3$V$_2$ Semiconductors: Cd$_3$P$_2$, Zn$_3$P$_2$, and Cd$_3$As$_2$, and Zn$_3$As$_2$. *Phys. Rev. B: Condens. Matter Mater. Phys.* **1994**, *50*, 7331.

(63) Jay-Gerin, J.-P.; Aubin, M. J.; Caron, L.-G. Energy-Band Structure and Electron Mobility of Cadmium Phosphide at Low Temperatures. *Phys. Rev. B: Condens. Matter Mater. Phys.* **1978**, *18*, 5675−5684.

(64) Xie, R.; Zhang, J.; Zhao, F.; Yang, W.; Peng, X. Synthesis of Monodisperse, Highly Emissive, and Size-Tunable Cd$_3$P$_2$ Nanocrystals. *Chem. Mater.* **2010**, *22*, 3820−3822.

(65) Glassy, B. A.; Cossairt, B. M. II$_3$V$_2$ (II: Zn, Cd; V: P, As) Semiconductors: From Bulk Solids to Colloidal Nanocrystals. *Small* **2017**, *13*, 1702038.

(66) Wu, K.; Liu, Z.; Zhu, H.; Lian, T. Exciton Annihilation and Dissociation Dynamics in Group II-V Cd$_3$P$_2$ Quantum Dots. *J. Phys. Chem. A* **2013**, *117*, 6362−6372.

(67) Wei, S.; Lu, J.; Yu, W.; Zhang, H.; Qian, Y. Isostructural Cd$_3$E$_2$ (E = P, As) Microcrystals Prepared via a Hydrothermal Route. *Cryst. Growth Des.* **2006**, *6*, 849−853.

(68) Katari, J. E. B.; Colvin, V. L.; Alivisatos, A. P. X-ray Photoelectron Spectroscopy of CdSe Nanocrystals with Applications to Studies of the Nanocrystal Surface. *J. Phys. Chem.* **1994**, *98*, 4109−4117.

(69) Adam, S.; Talapin, D. V.; Borchert, H.; Lobo, A.; McGinley, C.; de Castro, A. R. B.; Haase, M.; Weller, H.; Möller, T. The Effects of Nanocrystals Surface on the Luminescence Properties: Photoemission Study of HF-Etched InP Nanocrystals. *J. Chem. Phys.* **2005**, *123*, 084706.

(70) De Keukeleere, K.; Coucke, S.; De Canck, E.; Van Der Voort, P.; Delpech, F.; Coppel, Y.; Hens, Z.; Van Driessche, I.; Owen, J. S.; De Roo, J. Stabilization of Colloidal Ti, Zr, and Hf Oxide Nanocrystals by Protonated Tri-n-octylphosphine Oxide (TOPO) and Its Decomposition Products. *Chem. Mater.* **2017**, *29*, 10233−10242.

(71) Hanrahan, M. P.; Chen, Y.; Blome-Fernandez, R.; Stein, J. L.; Pach, G. F.; Adamson, M. A. S.; Neale, N. R.; Cossairt, B. M.; Vela, J.; Rossini, A. J. Probing the Surface Structure of Semiconductor Nanocrystals by DNP SENS with Dielectric Support Materials. *J. Am. Chem. Soc.* **2019**, *141*, 15532−15546.

(72) Hanrahan, M. P.; Stein, J. L.; Park, N.; Cossairt, B. M.; Rossini, A. J. Elucidating the Locations of Cd^{2+} in Post-Synthetically Treated InP Quantum Dots Using Dynamic Nuclear Polarization ^{31}P and ^{113}Cd Solid-State NMR Spectroscopy. *J. Phys. Chem. C* **2021**, *125*, 2956−2965.

(73) Holland, G. P.; Sharma, R.; Agola, J. O.; Amin, S.; Solomon, V. C.; Singh, P.; Buttry, D. A.; Yarger, J. L. NMR Characterization of Phosphonic Acid Capped SnO$_2$ Nanoparticles. *Chem. Mater.* **2007**, *19*, 2519−2526.

(74) Tomaselli, M.; Yarger, J. L.; Bruchez, M., Jr.; Havlin, R. H.; deGraw, D.; Pines, A.; Alivisatos, A. P. NMR Study of InP Quantum Dots: Surface Structure and Size Effects. *J. Chem. Phys.* **1999**, *110*, 8861−8864.

(75) Stein, J. L.; Holden, W. M.; Venkatesh, A.; Mundy, M. E.; Rossini, A. J.; Seidler, G. T.; Cossairt, B. M. Probing Surface Defects of InP Quantum Dots Using Phosphorus Kα and Kβ X-ray Emission Spectroscopy. *Chem. Mater.* **2018**, *30*, 6377−6388.

(76) Yakovkin, I. N.; Dowben, P. A. The Problem of the Band Gap in LDA Calculations. *Surf. Rev. Lett.* **2007**, *14*, 481−487.

(77) Perdew, J. P. Density Functional Theory and the Band Gap Problem. *Int. J. Quantum Chem.* **1985**, *28*, 497−487.

(78) Green, M.; O'Brien, P. The Synthesis of Cadmium Phosphide Nanoparticles Using Cadmium Diorganophosphide Precursors. *J. Mater. Chem.* **1999**, *9*, 243−247.

(79) Harris, R. K.; Becker, E. D.; Cabral de Menezes, S. M.; Goodfellow, R.; Granger, P. NMR Nomenclature: Nuclear Spin Properties and Conventions for Chemical Shifts: IUPAC Recommendations 2001. *Solid State Nucl. Magn. Reson.* **2002**, *22*, 458−483.

(80) Fung, B. M.; Khitrin, A. K.; Ermolaev, K. An Improved Broadband Decoupling Sequence for Liquid Crystals and Solids. *J. Magn. Reson.* **2000**, *142*, 97−101.

(81) Sakellariou, D.; Lesage, A.; Hodgkinson, P.; Emsley, L. Homonuclear Dipolar Decoupling in Solid-State NMR using Continuous Phase Modulation. *Chem. Phys. Lett.* **2000**, *319*, 253−260.

(82) Nuss, J.; Wedig, U.; Philippi, K.; Takagi, H. Dependence of the Physical Properties on the Cation Ordering in the New Ternary Phosphide ZnCu$_2$P$_8$. *Z. Anorg. Allg. Chem.* **2020**, *646*, 1144−1150.